Eur. Phys. J. A **27**, 243–256 (2006)
DOI 10.1140/epja/i2005-10267-y

THE EUROPEAN PHYSICAL JOURNAL A

Precision measurement of the coherent neutron scattering length of ^{3}He through neutron interferometry

W. Ketter[1,a], W. Heil[1], G. Badurek[2], M. Baron[2], E. Jericha[2], R. Loidl[2], and H. Rauch[2]

[1] Institut für Physik, Staudinger Weg 7, D-55099 Mainz, Germany
[2] Atominstitut der österreichischen Universitäten, Stadionallee 2, A-1020 Wien, Austria

Received: 20 April 2005 / Revised version: 21 February 2006 /
Published online: 29 March 2006 –
Communicated by Th. Walcher

Abstract. Improved knowledge of the real part of the neutron scattering length of ^{3}He is important for further development of nuclear few-body theory, as well as for a thorough understanding of neutron scattering off quantum liquids. The real part of the bound incoherent neutron scattering length $b'_{\rm i}$ has recently been measured directly with an experimental uncertainty of better than 1% by means of spin echo spectrometry. The uncertainty of the more fundamental bound multiplet scattering lengths $b'_{\pm}$ is thus limited by today's 1.2% uncertainty of the spin-independent coherent part $b'_{\rm c}$. Employing the skew-symmetric perfect crystal Si-interferometer at the S18 experimental site at ILL, Grenoble, we have re-measured the real part of the bound coherent neutron scattering length $b'_{\rm c}$ of ^{3}He. Our result $b'_{\rm c} = 6.010(21)$ fm exhibits a significant deviation compared to the latest accepted value $b'_{\rm c} = 5.74(7)$ fm (H. Kaiser, H. Rauch, G. Badurek, W. Bauspiess, U. Bonse, Z. Phys. A **291**, 231 (1979)). Including the known value of the incoherent neutron scattering length, we obtain new values for the real parts of the free singlet and triplet scattering lengths, $a'_- = 7.573(30)$ fm and $a'_+ = 3.480(18)$ fm. Our result contravenes by more than 7 standard deviations the measurement of the same physical quantity that has recently been performed by a group at NIST in a very similar experiment (P.R. Huffman, D.L. Jacobson, K. Schoen, M. Arif, T.C. Black, W.M. Snow, S.A. Werner, Phys. Rev. C **70**, 014004 (2004)) which yielded $b'_{\rm c} = 5.853(7)$ fm.

PACS. 21.45.+v Few-body systems – 27.10.+h $A \leq 5$ – 28.20.Cz Neutron scattering – 25.40.Dn Elastic neutron scattering

1 Introduction

Within the last decades, the conformity of theoretical predictions and experimental results for the observables of certain nuclear few-body systems have achieved a remarkable level of accuracy. For example, the s-wave neutron scattering lengths of the systems (n, D) [1,2] and (n, T) [3–7] are believed to be understood at the 10^{-3} level. On the other hand, since ^{3}He is a strong absorber for neutrons up to energies 1 eV [8], the (n, ^{3}He) system is more difficult to treat both theoretically as well as experimentally. For systems involving nuclei of spin $\boldsymbol{I}$, thermal neutron scattering will in general be described by spin-dependent scattering lengths $a_\pm$ which are assigned to the multiplet states of total spin $J = I \pm 1/2$. By scattering neutrons off a macroscopic and monatomic sample, the expectation value

$$\langle a \rangle = a_{\rm c} + a_{\rm i}\sqrt{\frac{I}{I+1}}\langle \boldsymbol{\sigma} \rangle \cdot \frac{\langle \boldsymbol{I} \rangle}{I}$$

is subject to observation, where by $\boldsymbol{\sigma}$ we denote the Pauli spin operator of the neutron. Herein, the spin-independent coherent ($a_{\rm c}$) and spin-dependent incoherent ($a_{\rm i}$) part of the scattering length are linear combinations of the more fundamental multiplet scattering lengths: defining statistical weight factors describing the degeneracy of the total spin states J,

$$g_+ = \frac{I+1}{2I+1}, \qquad g_- = \frac{I}{2I+1}, \tag{1}$$

the singlet (a_-) and triplet (a_+) scattering lengths are given by

$$a_- = a_{\rm c} - \sqrt{\frac{g_+}{g_-}}a_{\rm i}, \qquad a_+ = a_{\rm c} + \sqrt{\frac{g_-}{g_+}}a_{\rm i}. \tag{2}$$

In scattering theory it is convenient to consider the problem in the centre-of-mass system, where one defines

[a] *Current address:* Robert Bosch GmbH, Robert-Bosch-Str. 2, D-71701 Schwieberdingen, Germany;
e-mail: Wolfgang.Ketter@de.bosch.com

the scattering length a, referred to as the *free* scattering length. In the laboratory system, as the result of the reference frame transformation, it is common practice to use the so-called *bound* scattering length b given by $\frac{m_n}{\mu}a$, where m_n is the neutron mass and μ is the reduced mass of the neutron-target system.

Precise measurements of the spin-dependent neutron absorption in ^{3}He nuclei have already been performed in the 1960s [8]. These measurements pinpoint the imaginary part of the scattering length until the present day. In contrast, the real part of the coherent scattering length is only known at the percent level from unpolarized interferometry experiments [9]. Using experimental data of the free-scattering cross-section [10,11][1], the real parts of the multiplet scattering lengths could be derived on the 10% level. In a recent precision experiment, the incoherent part of the scattering length of the light isotope was determined to a relative uncertainty of 8×10^{-3} [13]. Although the result of this latter experiment has already attracted considerable interest [14], the situation is still unsatisfactory because the precision of the more fundamental multiplet scattering lengths is now strongly dominated by the uncertainty of the coherent part: in order to obtain balanced relative errors of the multiplet scattering lengths, $\frac{\delta b'_-}{b'_-} = \frac{\delta b'_+}{b'_+}$, the relative uncertainty of b'_c must be a factor of 4.3 below the corresponding incoherent quantity as a consequence of the linear combinations (2). Therefore, a relative uncertainty $\frac{\delta b'_c}{b'_c} = 3 \times 10^{-3}$ is required.

Moreover, other measurements of the scattering lengths of several isotopes (^{1}H: [15], ^{2}H: [16], Ar: [17], Kr and Xe: [18]) show considerable deviations compared to the values reported in [9]. Thus, there is reason to believe that in the case of ^{3}He, too, systematic errors have been underestimated in this latter work. We report here on a precise interferometric re-measurement of the bound coherent scattering length of ^{3}He that was undertaken to supply few-body theory with reliable and error-balanced values of the multiplet scattering lengths of ^{3}He.

2 Neutron refractive index

During the last decade, there seemed to be some confusion concerning the exact expression for the complex neutron refractive index in the low-energy limit. Several attempts [19,20] to express n as a function of the coherent scattering length in a way formally similar to the Goldberger-Seitz-formula [21] were either prone to violate the optical theorem or took into account only the leading contribution to the exact scattering cross-section, thereby neglecting terms of order $\mathcal{O}(k)$ and higher. On the other hand, apparative advances of the last years nowadays permit neutron optical precision experiments that demand at least the consideration of correction terms linear in k. We therefore begin with a discussion of the exact expression of the refractive index as a function of the coherent scattering length.

2.1 Sears' expression

According to [22], the neutron refractive index $n = n' + in''$ for neutrons having wave number k scattering off a sample of scattering center number density ϱ can be expressed in terms of the scattering amplitude $f = f' + if''$ as

$$n^2 = 1 + \frac{4\pi\varrho f}{k^2}\frac{1}{1-J}\,. \tag{3}$$

The local field correction J accounts for multiple scattering and vanishes for scattering off a dilute ideal gas. Since we have $\varrho\lambda^3 \ll 1$, $|kf| \sim 10^{-4}$ for thermal neutrons it follows that

$$\frac{\varrho}{k^2} f \ll 1.$$

Thus, the square root of (3) can be expanded to give

$$n = 1 + \frac{2\pi\varrho}{k^2} f + \mathcal{O}\left(\frac{\varrho^2|f|^2}{k^4}\right). \tag{4}$$

As is well known [23], the low-energy expansion of the (bound) scattering amplitude can be written in terms of the (bound) scattering length $b = b' - ib''$,

$$\begin{aligned} f &= -b + ikb^2 + \mathcal{O}(k^2) \\ &= [-b' + 2kb'b''] + i\left[b'' + k(b'^2 - b''^2)\right] + \mathcal{O}(k^2). \end{aligned} \tag{5}$$

Inserting this expression into (4), the neutron refractive index can be expressed as a function of the scattering length. Taking into account terms up to the order of k and splitting into the real and imaginary parts, we obtain

$$\begin{aligned} n = 1 &- \frac{2\pi\varrho}{k^2} b'(1 - 2kb'' + \mathcal{O}(k^2)) \\ &+ i\frac{2\pi\varrho}{k^2}(b'' + k(b'^2 - b''^2) + \mathcal{O}(k^2)). \end{aligned} \tag{6}$$

2.2 Beam losses due to n''

An exact expression for the neutron refractive index should contain both beam loss mechanisms, *i.e.* scattering losses as well as absorption losses, inherent in the optical theorem. In order to test this requirement, we now examine the imaginary part of expression (6), which is given by

$$n'' = \frac{\varrho}{2k}\left[\frac{4\pi}{k} b'' + 4\pi(b'^2 - b''^2) + \mathcal{O}(k)\right]. \tag{7}$$

As is shown in elementary scattering theory, *e.g.* [24], the differential scattering cross-section is given by the squared modulus of the scattering amplitude,

$$\frac{\mathrm{d}\sigma_\mathrm{s}}{\mathrm{d}\Omega} = |f(\theta)|^2. \tag{8}$$

[1] Alfimenkov's experiment measured the scattering cross-section of ^{3}He relative to ^{4}He and was re-analyzed by Guckelsberger taking into account improved values for the ^{4}He scattering [12].

Furthermore, Feenberg's optical theorem [25] connects the total cross-section $\sigma_\mathrm{t} = \sigma_\mathrm{a} + \sigma_\mathrm{s}$ (σ_a: absorption cross-section) to the imaginary part of the scattering amplitude in the forward direction,

$$\sigma_\mathrm{t} = \frac{4\pi}{k}\mathrm{Im}f(\theta = 0). \tag{9}$$

Inserting the scattering amplitude expansion (5) into (8) and (9), one readily obtains the cross-section expansions

$$\sigma_\mathrm{s} = 4\pi|b|^2(1 - 2kb'' + \mathcal{O}(k^2)), \tag{10}$$

$$\sigma_\mathrm{a} = \frac{4\pi}{k}b''(1 - 2kb'' + \mathcal{O}(k^2)). \tag{11}$$

Now the expression in square brackets of (7) can be written as the sum of (11) and (10):

$$\begin{aligned} n'' &= \frac{\varrho}{2k}\Big[\sigma_\mathrm{a} + 4\pi(b'^2 + b''^2) + \mathcal{O}(k)\Big] \\ &= \frac{\varrho}{2k}\Big[\sigma_\mathrm{a} + \sigma_\mathrm{s}\Big]. \end{aligned}$$

The scattering cross-section (10) includes coherent as well as incoherent scattering. For example, the bound scattering cross-section of an isotope of nuclear spin I with its spin-dependent scattering length

$$b = b_\mathrm{c} + \frac{b_\mathrm{i}}{\sqrt{I(I+1)}}\boldsymbol{\sigma}\cdot\boldsymbol{I} \tag{12}$$

is given by

$$\sigma_\mathrm{s} = 4\pi\left(|b_\mathrm{c}|^2 + |b_\mathrm{i}|^2 + \frac{2\mathrm{Re}(b_\mathrm{c}^* b_\mathrm{i})}{\sqrt{I(I+1)}}\boldsymbol{\sigma}\cdot\boldsymbol{I}\right), \tag{12a}$$

where we neglect terms in kb'' for clarity. The spin-independent part of this cross-section is the sum of the coherent and incoherent scattering cross-sections, which are defined by

$$\sigma_{\mathrm{s,c/i}} = 4\pi|b_\mathrm{c/i}|^2. \tag{13}$$

In an unpolarized experiment, $\langle\boldsymbol{\sigma}\cdot\boldsymbol{I}\rangle = 0$, the imaginary part of the refractive index is therefore related to the total reaction cross-section, *i.e.* the sum of the absorption as well as the coherent and incoherent scattering cross-sections:

$$\begin{aligned} n'' &= \frac{\varrho}{2k}\Big[\sigma_\mathrm{a} + \sigma_\mathrm{s,c} + \sigma_\mathrm{s,i}\Big] \\ &= \frac{\varrho}{2k}\sigma_\mathrm{t}. \end{aligned}$$

We therefore see that the imaginary part of our expression (6) indeed satisfies the optical theorem. For scattering thermal neutrons off ^{3}He, the total cross-section is strongly dominated by the absorption cross-section [26],

$$\begin{aligned} &\sigma_\mathrm{a} = 5327^{+10}_{-9}\,\mathrm{b}, \\ &\sigma_\mathrm{s,c} + \sigma_\mathrm{s,i} = 3.4(2)\,\mathrm{b}. \end{aligned}$$

Thus, to an excellent approximation,

$$n'' \approx \frac{\varrho}{2k}\sigma_\mathrm{a}. \tag{14}$$

For thermal neutrons we can emphasize the linear wavelength dependence of the absorption cross-section by explicitly factorizing

$$\sigma_\mathrm{a}\,[\mathrm{barn}] = 5327^{+10}_{-9} \times \frac{\lambda}{1.798\,\text{Å}} \equiv \lambda \cdot K_\mathrm{a}. \tag{15}$$

3 Experimental procedure

Interferometry is presumably the most straightforward way to measure refractive indices of sufficiently transparent materials. This technique has nowadays become a standard procedure also for neutron optical experiments [27–29]. Compared to the very first interferometric refractive-index measurements [9], today's experiments benefit from increased neutron flux as well as improved crystal quality, crystal shape, and thermal as well as mechanical stability of the apparatus.

Out of the thermal neutron beam at the H25 neutron guide at ILL, nearly monoenergetic neutrons are reflected from a perfect silicon monochromator crystal through several slits onto the instrument. The interferometer is positioned in a such way that the Bragg reflecting [220] lattice planes of the monochromator and the interferometer's slabs form a nondispersive setup, cf. fig. 1. Inside the first slab, the normalized incident neutron's wave function ψ is divided by amplitude into two coherent partial wave functions $\psi_{1,2}$ which subsequently travel through the interferometer via spatially separated paths. At the location of the last silicon slab, the partial wave functions interfere coherently and form two outgoing wave functions

$$\psi_\emptyset = \psi_1 + \psi_2, \qquad \psi_H = \psi_1 - \psi_2$$

which, without beam losses, are again normalized so that

$$|\psi_\emptyset + \psi_H|^2 = 1. \tag{16}$$

When a sample of refractive index n' and thickness s is brought into one of the paths, say path 2, the phase of partial wave function ψ_2 travelling with wave number k will be shifted according to

$$\phi_{n'} = (n' - 1)ks \tag{17}$$

with respect to ψ_1. Inserting the real part of (6) into (17), we get the important relation

$$\phi_{n'} = -\varrho s\lambda b'_\mathrm{c}(1 - 2kb''_\mathrm{c} + \mathcal{O}(k^2)), \tag{18}$$

where we have limited our attention to the unpolarized case, $\langle\boldsymbol{\sigma}\cdot\boldsymbol{I}\rangle = 0$. If we neglect the k^2 correction within the brackets, which is of the order 10^{-8}, relation (18) states that the phase shift $\phi_{n'}$ is essentially a linear function of the wavelength of the neutron, the coherent scattering length of the nuclei and the sample's gas particle number density per unit area. Hence, if the neutron wavelength and the sample thickness are known, the scattering length can be measured as a change in phase shift when the particle number density is altered. This is the central idea of the experiment described here.

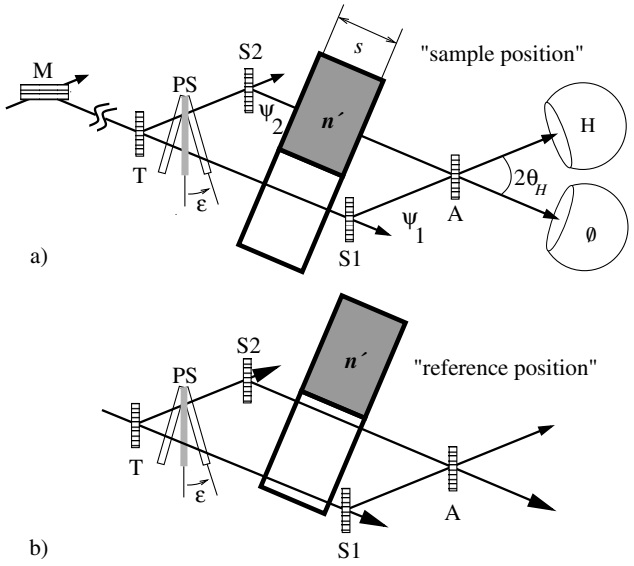

Fig. 1. A thermal neutron beam is reflected by a monochromator crystal towards the interferometer. The neutron wave function is divided by amplitude within the divider slab T. The partial wave functions $\psi_{1,2}$ travel spatially separated through the instrument. They are reflected by mirror slabs S1, S2 towards the analyzer slab A where they interfere coherently. The crystal's reflecting lattice plane orientations are shown by thin lines. The outgoing wave function is detected in two ^{3}He counters $\emptyset$, H. The sample, which is characterized by the refractive index n', was either placed in one of the partial neutron beams or removed from both partial beams. In the "sample" position a) the phase shift due to the sample can be detected, while the phase shift due to the aluminum windows is largely compensated by the evacuated reference cell. In the "reference" position b) the intrinsic phase shift $\phi_{\rm int}$ of the instrument can be monitored. By rotation of an aluminum phase shifter PS through an angle ε, the relative phase $\phi_{\rm ps}$ of the partial beams can be controlled. $\varepsilon = 0$ is assigned to the symmetrical position of the aluminum flag, where the phase shift $\phi_{\rm ps}$ vanishes.

Besides the sample's phase shift, there are three additional contributions to the total phase shift of the partial beams. Firstly, it turns out that the sample cell itself causes a constant phase shift offset $\phi_{\rm int}^{\rm offset}$, which can be explained by slight window thickness imperfections of the sample container and is observed in the sample position *relative* to the reference position. Secondly, we observe that the instrument gives rise to a time-varying phase shift $\phi_{\rm int}(t)$ due to mechanical and thermal instabilities. We will return to discuss these so-called intrinsic phase shifts below. Finally, we add an adjustable phase shift $\phi_{\rm ps}$ by means of a plane parallel aluminum phase flag, cf. fig. 1. We rotated the phase shifter through 32 orientations ε_i, thereby varying the relative phase between the two partial wave functions over $-2\pi \lesssim \phi_{\rm ps}(\varepsilon_i) \lesssim +2\pi$ with

$$\phi_{\rm ps}(\varepsilon_i) = 2\pi\Big(\sec(\theta_H - \varepsilon_i) - \sec(\theta_H + \varepsilon_i)\Big)\frac{D_{\rm ps}}{D_\lambda}. \quad (19)$$

$D_{\rm ps}$ is the thickness of the phase shifter, $2\theta_H$ is the angle between the two partial beams after the divider slab and D_λ is the λ-thickness of aluminum given by $D_\lambda = \frac{\lambda}{n'_{\rm ps}-1}$ which is about $\sim 150\,\mu$m for thermal neutrons, $\lambda = 1.9\,$Å. In each phase shifter orientation, neutrons were counted in both detectors for a period of $\Delta t = 10\,$s. As a result, we record intensity signals, so-called interferograms, which are sinusoidally oscillating functions of the phase flag rotation angle. To summarize, the total phase shift of the partial beams is given by

$$\Phi = \phi_{n'} + \phi_{\rm ps}(\varepsilon_i) + \phi_{\rm int}^{\rm offset} + \phi_{\rm int}(t). \quad (20)$$

The total phase shift (20) is detectable as an intensity modulation of the two outgoing beams

$$I_{\emptyset,H} \propto |\psi_{\emptyset,H}|^2 = (1 \pm \cos\Phi)/2,$$

where the upper(lower) sign is valid for the $\emptyset(H)$ beam, respectively.

If one of the partial neutron beams inside the interferometer passes a neutron absorbing material like ^{3}He, eq. (16) is not valid anymore. Nevertheless, absorption only has the effect of reducing the mean outgoing neutron intensity and the visibility of the interference fringes without changing the phase relation of the transmitted partial waves. Then the phase-dependent intensity oscillations read

$$I_{\emptyset,H} = (1 + \gamma \pm 2\sqrt{\gamma}\cos\Phi)/4, \quad (21)$$

where extinction mechanisms are described by the damping factor

$$\gamma := \exp(-2n''ks) = \exp(-K_{\rm a}\varrho s\lambda). \quad (22)$$

In our discussion we have not yet considered that the relative intensities of the two partial beams can be different, *i.e.*

$$|\psi_1|^2 \neq |\psi_2|^2.$$

Starting from a normalized incident neutron flux, the resulting partial-beam intensities $I_{1,2} = |\psi_{1,2}|^2$ depend on both the reflectivity and transmittivity of the interferometer's divider slabs (cf. fig. 1) which may even vary slightly in time due to detuning of the instrument's adjustment caused by thermal drifts or mechanical shocks, for example. Thus, we have to replace (21) by

$$I_{\emptyset,H} = (I_1 + \gamma \cdot I_2 \pm 2 \cdot \sqrt{I_1 \cdot I_2 \cdot \gamma}\cos\Phi)/4. \quad (23)$$

In particular, the total outgoing beam intensity $I_{\rm out}$ is a function of the relative partial-beam intensities $I_{1,2}$:

$$I_{\rm out} = I_\emptyset + I_H = I_1 + \gamma \cdot I_2. \quad (24)$$

As described in more detail in sect. 3.6 the pressure-dependent ratio

$$T = I_{\rm out}^{\rm sam}/I_{\rm out}^{\rm ref} = \frac{I_1 + \gamma \cdot I_2}{I_1 + I_2} \quad (25)$$

of the outgoing-beam intensities in the sample (sam) and reference (ref) position (cf. fig. 1) can be used to determine directly the damping factor γ and with it the product term $\varrho \cdot s \cdot \lambda$, cf. (22). The latter quantity is needed

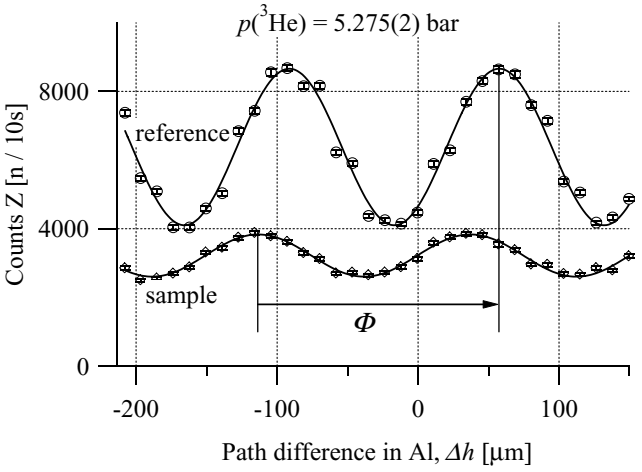

Fig. 2. Interference fringes recorded in the ∅ detector when one of the partial beams travels through the sample cell (bottom) and when both beams travel through the evacuated reference cell (top). The phase shift Φ is greater than 2π for sample pressures above ~ 4.5 bar.

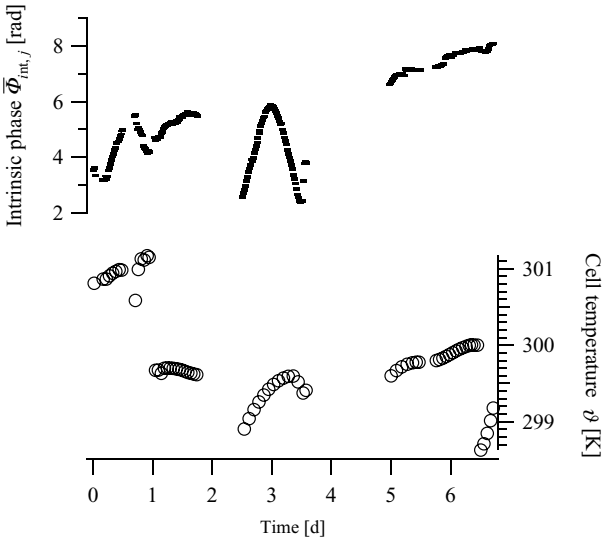

Fig. 3. The intrinsic phase of the instrument over the complete beam time is obviously correlated with the temperature of the instrument. Violations of the correlation, *e.g.* at $t = 1$ d, are caused by mechanical modifications of the setup.

in order to extract the coherent scattering length b'_c from the measured phase shift $\phi_{n'}$ (cf. sect. 3.4). In order to measure the phase shift due to the sample, a pair of interferograms was recorded with and without the sample in the path of the partial wave function ψ_2, see fig. 2. For the sake of brevity, we refer to the sample interferogram (lower intensity in fig. 2 due to neutron absorption within the sample) when the partial beam 2 passes the sample cell, cf. fig. 1a). When both partial beams pass through the evacuated compensation cell, fig. 1b), we speak of the reference interferogram (higher intensity in fig. 2).

We now discuss the time dependence of the intrinsic phase shift $\phi_{\rm int}(t)$. Let Δt be the integration time of an individual measurement at time t_i. Then the mean intrinsic phase shift during this measurement is given by

$$\phi_{\rm int}^{\Delta t}(t_i) = \int_{t_i}^{t_i+\Delta t} \frac{\partial \phi_{\rm int}(t)}{\partial t}\,{\rm d}t. \tag{26}$$

In the reference position one observes for a given phase shifter position ε_i the total phase shift

$$\phi_i^{\rm ref} = \phi_{\rm ps}(\varepsilon_i) + \phi_{\rm int}^{\Delta t}(t_i). \tag{27}$$

The time dependence of the intrinsic phase shift can be analyzed as follows: we choose the *ansatz*

$$\phi_{\rm int}^{\Delta t}(t_i) = f(t_i) + g(t_i),$$

where $g(t_i)$ behaves statistically in the sense that it satisfies $\langle g(t_i)\rangle_T = 0$ over the measuring period T of a complete interferogram. The remaining term can be expanded to a polynomial of order M:

$$f(t_i) = \sum_{k=0}^{M} q_k \cdot (t_i)^k. \tag{28}$$

Now Δt and T are chosen such that during the period T

$$\phi_{\rm int}(t_i) = q_0 + q_1 \cdot t_i + g(t_i) \tag{29}$$

is valid to very good approximation. We verified experimentally that this was the case for $\Delta t = 10$ s and $T \approx 10$ min: Higher-order polynomial terms in the measured phase shifts $\phi_i^{\rm ref}$, eq. (27), would become noticeable in the interferograms as the fit function within the experimental error bars would deviate from a pure sine (cf. fig. 2), and this was definitely not observed. Long-term drifts, *i.e.* nonlinear contributions

$$\tilde{f}(T_j) = \sum_{k=2}^{M} q_k \cdot (T_j)^k \tag{30}$$

only could be traced by analyzing sequences of interferograms j over periods of days and plotting the extracted intrinsic phases $\overline{\phi}_{{\rm int},j}$ *vs.* time, cf. fig. 3. A comparison with the ambient temperature of the interferometer, also plotted in cf. fig. 3 for the complete course of the measurements, shows that the intrinsic phase of the instrument is obviously correlated to the temperature of the interferometer. It is thus necessary to stabilize the temperature of the instrument to reduce these unwanted phase drifts. The data shown in fig. 3 were recorded using a thermally isolated and stabilized setup, which will be described in sect. 3.2. After stabilization, linear intrinsic phase drifts up to $q_1 \leq \pi/(12)$ h were observed.

Since the sample interferogram contains the intrinsic phase shift as well,

$$\phi_i^{\rm sam} = \phi_{n'} + \phi_{\rm ps}(\varepsilon_i) + \phi_{\rm int}^{\rm offset} + \phi_{\rm int}^{\Delta t}(t_i), \tag{31}$$

a sequential recording of both interferograms was not feasible with our setup due to thermal drifts which may generate additional phase shifts falsely assigned to $\phi_{n'}$ of the sample. During the time $T \approx 10$ min necessary to record a

complete interferogram the intrinsic phase may change as much as 40 mrad, if the maximum observed thermal variation of the temperature stabilized instrument is assumed. To compensate this intrinsic phase drift each pair of interferograms (reference and sample) was recorded pseudo-simultaneously. This means that for each phase shifter orientation, the sequence of sample and reference measurements is reversed. If for a given phase shifter position neutrons were counted first in the cell's sample position and afterwards in the reference position, then after rotating the phase shifter to the next orientation, neutrons were counted first in the cell's reference and subsequently in the sample position. A simulation calculation was carried out in order to estimate the residual systematic effect on the sample phase $\phi_{n'}$ under worst case conditions, *i.e.* $q_1 = 40\,\mathrm{mrad}/(10\,\mathrm{min})$, when this pseudo-simultaneous measuring sequence is used.

3.1 Eliminating systematics due to linear intrinsic phase drifts

For N phase shifter positions ε_i the corresponding values of the phases $\phi_{\mathrm{ps}}(\varepsilon_i)$ are generated using 19. This data set gives the phase shifter's contribution at position ε_i to the total phase of both the reference and sample interferogram. The sample interferogram phases are then shifted by adding a fixed value of $\phi_{n'}$, the sample's phase contribution. The contribution of the linear phase drift q_1 is taken into account by adding the intrinsic phase $q_0 + q_1 \cdot \tau_1$ to the j-th data point of this pseudo-simultaneous measurement sequence, where τ_j reflects the start time of the j-th measurement ($1 \le j \le 2N$). The values of τ_j are not equidistantly spaced: After a counting time $\Delta t_{\mathrm{count}} = 10\,\mathrm{s}$, either the phase shifter is moved to its next position, which takes $\Delta t_{\mathrm{ps}} = 6\,\mathrm{s}$ or the twin cell is moved from the reference to the sample position or vice versa with $\Delta t_{\mathrm{rs}} = 18\,\mathrm{s}$. Figure 4 shows a timing diagram of such a measurement sequence starting with the reference measurement at phase shifter position ε_i. The expected total phases at time τ_j then follow the scheme:

$$\begin{aligned}
\Phi_1^{\mathrm{ref}} &= \phi_{\mathrm{ps}}(\varepsilon_1) + q_0 + q_1\tau_1,\\
\Phi_1^{\mathrm{sam}} &= \phi_{n'} + \phi_{\mathrm{ps}}(\varepsilon_1) + q_0 + q_1\tau_2,\\
\Phi_2^{\mathrm{sam}} &= \phi_{n'} + \phi_{\mathrm{ps}}(\varepsilon_2) + q_0 + q_1\tau_3,\\
\Phi_2^{\mathrm{ref}} &= \phi_{\mathrm{ps}}(\varepsilon_2) + q_0 + q_1\tau_4,\\
\Phi_3^{\mathrm{ref}} &= \phi_{\mathrm{ps}}(\varepsilon_3) + q_0 + q_1\tau_5,\\
&\cdots \quad .
\end{aligned}$$

Now, the two sets of N values for the total phases $\Phi_i^{\mathrm{ref(sam)}}$ are used to simulate the data points $Z_i^{\mathrm{ref(sam)}}$ of an interferogram like in fig. 2 by taking the simple relation

$$Z_i^{\mathrm{ref(sam)}} = \cos \Phi_i^{\mathrm{ref(sam)}}. \tag{32}$$

The generated data of both the reference and sample interferogram are finally fitted using the model function

$$Z = K_1 + K_2 \cos(K_3 \cdot (\phi_{\mathrm{ps}} - \phi_0) + K_4). \tag{33}$$

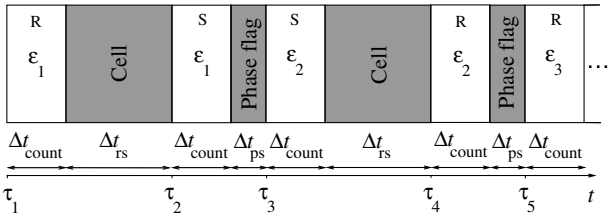

Fig. 4. Timing diagram of the measurement sequence. Counting times are shown as white boxes, whereas times of adjustments are shaded grey. The sequence of measurements in the reference and the sample position alternate from one phase shifter position (ε_i) to the next (ε_{i+1}).

The fit parameters K_1 and K_2 have been included for simple plausibility tests. They should of course agree reasonably well with $K_1 = 0$ and $K_2 = 1$. While ϕ_{ps} is the independent variable, ϕ_0 has been introduced in order to vary the start phase between different simulations within $-\pi \le (\phi_0 - \overline{\phi}_{\mathrm{ps}}) \le +\pi$, where the mean value of the phase shifter phases $\overline{\phi}_{\mathrm{ps}}$ is given by

$$\overline{\phi}_{\mathrm{ps}} = \frac{1}{2}\left(\phi_{\mathrm{ps}}(\varepsilon_N) + \phi_{\mathrm{ps}}(\varepsilon_1)\right).$$

The $N = 32$ values of the phase shifter phases $\phi_{\mathrm{ps}}(\varepsilon_i)$ always span a range of $[-2.5\pi, 2.5\pi]$. By taking the difference of the fitted phases K_4 of the two interferograms, we get an estimate for the input parameter $\phi_{n'}$. The deviation of this estimate from the input value $\phi_{n'}$ is then given by

$$\Delta\phi_{n'} = K_{4,\mathrm{sam}} - K_{4,\mathrm{ref}} - \phi_{n'}. \tag{34}$$

Furthermore, calculations have been carried out for several fixed values of the sample phase shift $0 \le \phi_{n'} \le 2\pi$. A linear phase drift of slope $q_1 = 10^{-4}$ rad/s was assumed in all calculations, corresponding to the largest value that was observed during the experiment. Without loss of generality, q_0 was set to zero. Each pair of data sets was fitted using different values of the start phase ϕ_0.

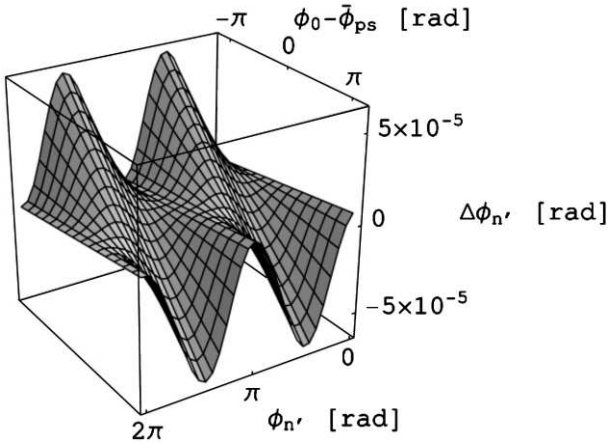

Fig. 5. Systematical phase fit error $\Delta\phi_{n'}$ due to a linear phase drift as a function of the true phase shift $\phi_{n'}$ of the sample and of the deviation $\phi_0 - \overline{\phi}_{\mathrm{ps}}$ of the fit reference phase with respect to the center of the data.

Figure 5 shows the deviations $\Delta\phi_{n'}$ as a function of the input parameter $\phi_{n'}$ and as a function of the difference $\phi_0 - \overline{\phi}_{\rm ps}$. The systematical phase error due to phase drifts is of the form $\Delta\phi_{n'} \propto -(\phi_0 - \overline{\phi}_{\rm ps}) \sin^2 \phi_{n'}$ and vanishes when the fit start phase is set to the center of the data, $\phi_0 = \overline{\phi}_{\rm ps}$. Even under the assumption that the fit start phase is shifted by as much as half a period away from the center of the interferogram, the deviation $\Delta\phi_{n'}$ is well below 5×10^{-5} rad. We thus get the important result that the systematical error stemming from linear phase drift can in principle be eliminated completely if the start phase ϕ_0 of the harmonic fit is set to the mean phase shifter phase $\overline{\phi}_{\rm ps}$. Application of this technique is tacitly assumed in the data analysis which will be described in sect. 4.

3.2 Apparatus

The skew-symmetrically shaped interferometer crystal is placed on a rotatable table which is equipped with a piezo stepper and an encoder which allow angular adjustment of the crystal with a resolution of 0.2 μrad within 110 mrad. Together with the monochromator crystal, the interferometer table is mounted on a suspended optical bench that provides excellent vibration damping. The phase shifter, an aluminum slab of 5 mm thickness and plane parallel surfaces, can be positioned to an accuracy of 1 μrad by a goniometer. The neutrons in the $\emptyset$- and H-beams are counted in two ^{3}He filled detectors. A concise description of the basic instrument setup S18 can be found in [30].

A cylindrical volume containing the interferometer table, the interferometer crystal itself, the twin cell and the phase shifter, was thermally isolated by wrapping it with a double layer of Mylar© foil. This box was thermally regulated using a combined system of a 120 W electrical heating and a double water cooling cycle, which is stabilized to the cooling water temperature.

3.3 Wavelength

The mean neutron wavelength was determined by measuring the rotation angle 2θ of the interferometer to the symmetrical Bragg peak, where the [220] lattice planes of the monochromator and the interferometer slabs form a dispersive setup, cf. fig. 6. Using the lattice constant of silicon $d_H = 1.92005(2)$ Å [31], and the well-known Bragg condition for the reflection of first order $\lambda/2 = d_H \sin\theta$, the mean wavelength of the neutrons was found to be

$$\lambda = 1.910(2)\,\text{Å}. \tag{35}$$

The uncertainty of this value is dominated by the diffuse peak position of the dispersive Bragg peak, see fig. 6. We examined the sensitivity of the fitted peak position to both cuts at the left and right tails of the peak and the way background was subtracted from the measured rocking curve of the dispersive Bragg peak. It could be shown that the dispersive peak position is uncertain by less than 0.03°, cf. table 1.

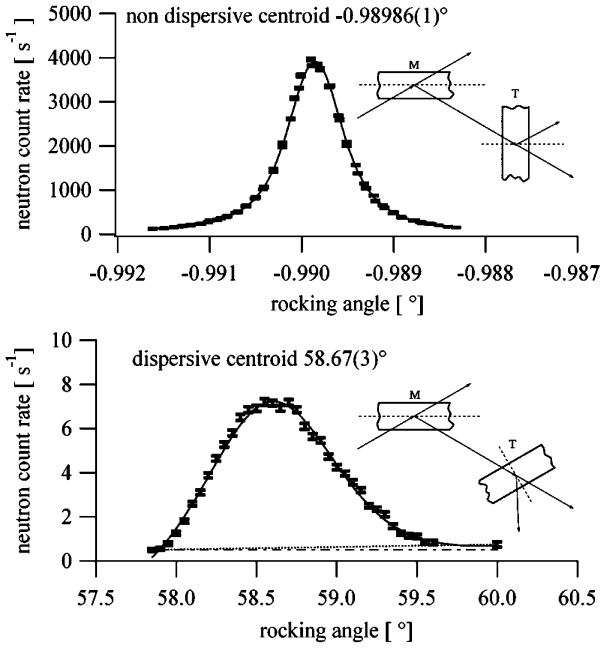

Fig. 6. Rocking curves of the dispersive and nondispersive Bragg peaks. When the lattice planes of the monochromator crystal and the interferometer crystal are coplanar, the beam is Bragg reflected at the interferometer slabs and both crystals form a nondispersive setup (top). When the interferometer crystal is rotated by two Bragg angles around an axis perpendicular to the incidence plane, the Bragg condition is again fulfilled and both crystals form a dispersive setup (bottom). The mean neutron wavelength can be computed from a measurement of the interferometer rotation angle between the two Bragg peaks. The data are well described by Voigt functions (solid lines). Different backgrounds (dotted lines) were subtracted from the low-intensity dispersive data to investigate the uncertainty of the peak position.

Table 1. Dependence of the dispersive peak's position on subtraction of different background models and the data cuts at the low- and high-angular tail of the rocking curve.

	Centroid $\alpha_{\rm disp}$
Raw data	58.681°
Constant background	58.669°
Linearly increasing background	58.669°
Cut data points $\alpha_{\rm disp} \geq 59.4°$	58.649°
Cut data points $\alpha_{\rm disp} \leq 58.0°$	58.692°
Cut data points $\alpha_{\rm disp} \geq 59.4°$, $\alpha_{\rm disp} \leq 58.0°$	58.659°
Mean centroid	58.67(3)°

3.4 Admixture of λ/n neutrons

It is a general property of monochromator crystals that λ/n-contaminations ($n = 2, 3, \ldots$) are also present in the reflected beam. Starting from (17) it is easily shown that the mean phase shift of nonmonochromatic beams is given by $\overline{\Phi} = (n' - 1)\frac{2\pi}{\overline{\lambda}} s$, where the mean wavelength

of the beam's particles is given by $\overline{\lambda} = \sum_{n=1}^{N} a_{\frac{\lambda}{n}} \frac{\lambda}{n}$ with $\sum_{n=1}^{N} a_{\frac{\lambda}{n}} = 1$. The relative weights $a_{\frac{\lambda}{n}}$ of λ/n neutrons generally decrease with increasing n because of the λ-dependence of the nuclear structure factor resulting in lower peak reflectivity. Due to multiple Bragg reflection at the Si-interferometer slabs higher-order wavelength contaminations are still more suppressed. Moreover, the thermal neutron flux at the neutron guide H25 at ILL rapidly drops off for neutron wavelengths $\lambda < 1.5\,\text{Å}$, so we expect higher-order contaminations to be negligibly small. However, due to the $(1/v)$-law of absorption, the relative admixture of λ/n neutrons grows when the optical thickness of the absorber (^{3}He) is increased.

For a more quantitative analysis of higher-order contaminations it is sufficient to assume that the neutron beam traveling through the interferometer is an admixture of a_λ neutrons of wavelengths λ and $a_{\frac{\lambda}{2}}$ neutrons of wavelength $\lambda/2$ satisfying $a_\lambda + a_{\frac{\lambda}{2}} = 1$. Then, the initial mean wavelength of the neutron beam is given by $\overline{\lambda}_\mathrm{i} = \frac{1+a_\lambda}{2}\lambda$. After having traveled through an absorbing sample characterized by s and n'', cf. eq. (17), the neutrons of wavelength λ will be attenuated to a fraction γa_λ, while neutrons of wavelength $\lambda/2$ will only be reduced to $\sqrt{\gamma} a_{\frac{\lambda}{2}}$, where $\gamma = \exp(-K_\mathrm{a}\varrho s\lambda)$ as before, cf. eq. (22). Calculation of the final mean wavelength $\overline{\lambda}_\mathrm{f}$ behind the absorbing sample yields

$$\overline{\lambda}_\mathrm{f} = \frac{\sqrt{\gamma}\frac{a_\lambda}{1-a_\lambda} + \frac{1}{2}}{\sqrt{\gamma}\frac{a_\lambda}{1-a_\lambda} + 1}\lambda. \tag{36}$$

Even for a small initial $\lambda/2$ contamination $1 - a_\lambda \ll 1$, the mean final wavelength $\overline{\lambda}_\mathrm{f}$ will eventually approach $\lambda/2$ for strong absorption, $\gamma \to 0$.

This change of the detected neutrons' mean wavelength clearly alters the simple linear number density dependence of the phase shift (18). Rather, replacing λ in (18) by $\overline{\lambda}_\mathrm{f}$, we get

$$\begin{aligned}\phi_{n'} &= -\overline{\lambda}_\mathrm{f}\varrho s b'_\mathrm{c}(1 - 2k b''_\mathrm{c}) \\ &= \frac{\sqrt{\gamma}\frac{a_\lambda}{1-a_\lambda} + \frac{1}{2}}{\sqrt{\gamma}\frac{a_\lambda}{1-a_\lambda} + 1}\lambda\varrho s b'_\mathrm{c}(1 - 2k b''_\mathrm{c}),\end{aligned} \tag{37}$$

where we have neglected the correction to the small term in $k b''_\mathrm{c}$ for brevity.

Measuring the phase shift as a function of the number density therefore enables one to detect higher-order wavelength contaminations as deviations from the strictly linear behaviour (18). Since $b''_\mathrm{c} = -1.4816(28)\,\text{fm}$ [32][2] and γ is a well-known function of ϱs, cf. eq. (22), the relative weight a_λ of λ-neutrons within the initial beam can be quantified using the model function (37).

[2] The errors of the imaginary parts of the scattering lengths that have been stated in this publication were underestimated by a factor of 10 [33].

3.5 Cell design

The container for the gaseous sample should have a constant effective sample thickness over the partial neutron beam cross-section. The neutron beam windows of the container must be highly plane parallel in order to conserve coherence over the neutron beam cross-section. Our windows were made from aluminum which has a lambda-thickness of 150 μm for neutrons of wavelength $\lambda = 1.9\,\text{Å}$. The plane parallelism ($< 8\,\mu$m over the neutron beam diameter), the flatness ($< 6\,\mu$m) and the roughness ($R_\mathrm{max} < 3\,\mu$m) of the fine-cut window surfaces were much smaller than the lambda thickness of the window material to avoid decoherence. The rather large value of nonparallelism is the consequence of a slightly biconcave shape of the window thickness which was unavoidable in the manufacturing process. Although neutron coherence conservation is assured, the variation of the aluminum window thickness leads to an offset phase shift which will be discussed in sect. 4. The aluminum window thickness was chosen to be 6 mm which is sufficient to limit window bending under pressures of up to 10 bar below 6 μm. The deformation of the sample cell under pressure was investigated experimentally and yields

$$s = 38.017\,\text{mm} + (0.002\,\text{mm/bar}) \cdot p \pm 0.008\,\text{mm} \tag{38}$$

at $\vartheta = 26.6(1.3)\,^\circ\text{C}$, where the additional effects of thermal expansion of the cell material are already included. The phase shift of the sample beam inside the window material must be compensated to preserve coherence of both partial beams. This is done by placing an identical but evacuated cell into the second partial beam. To avoid misalignment, both cells were combined to one twin vessel milled from a single aluminum block, cf. fig. 7. Moreover, also the entrance and exit windows were realized as single pieces for both cells to ensure optimal parallelism. The helium leakage rate of both cells was measured to be less than $10^{-8}\,\text{mbar}\ell/\text{s}$, resulting in a pressure change below $10^{-2}\,\text{mbar/day}$. The skew symmetry of the interferometer

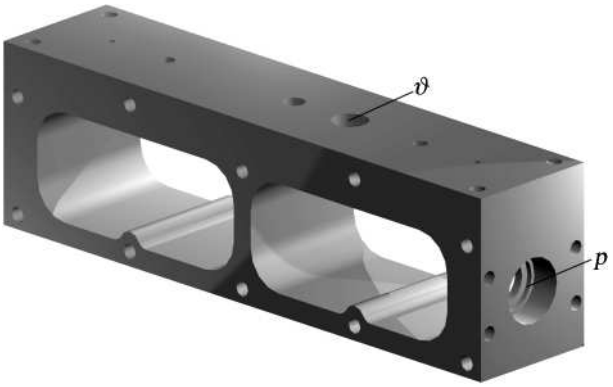

Fig. 7. Aluminum body of the twin cell. Both chambers have dimensions $38 \times 70 \times 30\,\text{mm}^3$ (L×W×H). Plane parallel aluminum windows are screwed on the face ends and sealed with O-rings. The sample chamber has two retainers for a pressure gauge (p) and a temperature sensor (ϑ).

leads to nearly parallel partial beams inside the instrument. Thus, the twin cell does not act as a phase shifter: if the partial neutron beams do not hit the cell orthogonally, the effective window thickness is still equal in both partial beams. Therefore, a potential misalignment δ of the twin cell does not cause systematical phase contributions. On the other hand, the increasing effective sample thickness $s_{\mathrm{eff}} = s/\cos\delta$ leads to a second-order systematic effect. Even for a cell misalignment δ as large as 2.5°, which could easily be detected, the increase of the effective cell thickness is smaller than $10^{-3} \times s$ and is thus negligible. Cell misalignment during the experiment was smaller than 1°, which was verified using a theodolite.

3.6 Particle number density

The sample chamber of the twin cell has two retainers where sensors to measure the gas pressure p and the gas temperature ϑ were fixed. The ceramic pressure gauge Bourdon Haenni EL74 and the semiconductor temperature transducer National Semiconductor LM35AH were calibrated twice by the German Calibration Service (DKD). The calibrations were performed at the time of the experiment and two years later: both times, the transducers were mounted at the cell and they have not been removed in between. The signals of both sensors were found to deviate within the limits claimed by the manufacturers. The signal of the LM35AH exhibited systematic deviations of $\Delta\vartheta_{\mathrm{m}} \equiv \vartheta_{\mathrm{m}} - \vartheta_{\mathrm{cal}} = -0.24\,\mathrm{K}$ in 2003 and $\Delta\vartheta_{\mathrm{m}} = -0.44\,\mathrm{K}$ in 2005 at room temperature. We assumed an uncertainty of $\sigma_{\vartheta_{\mathrm{m}}} = 0.5\,\mathrm{K}$, which is the conservative estimate provided by the manufacturer for the uncalibrated transducer. The output signal of the EL74 pressure transducer showed a systematic deviation $\Delta p_{\mathrm{m}} \equiv p_{\mathrm{m}} - p_{\mathrm{cal}}$ of less than $\frac{\Delta p_{\mathrm{m}}}{p_{\mathrm{m}}} < -0.4\%$ over the complete pressure range $(0, \ldots, 10\,\mathrm{bar})$. From a parabola fit $f(p_{\mathrm{m}})$ to the data points of the 2003 calibration, cf. fig. 8, we could correct the EL74 readout pressure according to

$$p_{\mathrm{cal}} = p_{\mathrm{m}} \cdot (1 - f(p_{\mathrm{m}}))\,. \tag{39}$$

As a conservative estimate of the pressure uncertainty we used the relative deviation of the 2003 and 2005 calibration data, *i.e.* $\Delta p_{\mathrm{m}}/p_{\mathrm{m}} = \pm 0.2\%$, see fig. 8. Measuring the thermodynamic variables p and ϑ of the sample gas, the particle number density ϱ can be calculated from the van der Waals equation for real gases

$$\left(p + \frac{a\varrho^2}{N_{\mathrm{A}}^2}\right)\left(1 - \frac{\varrho}{N_{\mathrm{A}}}b\right) = \frac{\varrho}{N_{\mathrm{A}}}R\vartheta, \tag{40}$$

which is a cubic equation in ϱ. N_{A} denotes Avogadro's number, R is the molar gas constant, and the van der Waals constants for helium are given by $a = 34.6077(12) \times 10^{-9}\,\mathrm{bar\,m^6/mol^2}$ and $b = 23.7384(6) \times 10^{-6}\,\mathrm{m^3/mol}$ [31].

With the particle number density ϱ, the effective sample thickness s, eq. (38), and the mean wavelength λ, eq. (35) we can finally determine the product term $\varrho \cdot s \cdot \lambda$ and with it the damping factor γ, eq. (22). As was already discussed before, by measuring the total outgoing beam intensities $I_{\mathrm{out}}^{\mathrm{sam}}$, $I_{\mathrm{out}}^{\mathrm{ref}}$ in the sample and reference position, respectively, we get an independent access to these quantities. Thus the transmission measurements provide a cross-check for the correctness of the product term as derived from the individual quantities ϱ, s, and λ. In fig. 9 the transmission T as calculated from the summed neutron counts in the sample and reference positions, see eq. (25), is plotted as a function of the sample gas particle number per unit area, $\varrho \cdot s$. Discontinuities, which are significant within the error bars, indicate that the partial-beam intensities $I_{1,2}$ were not constant during the whole measurement period of almost 170 hours. There-

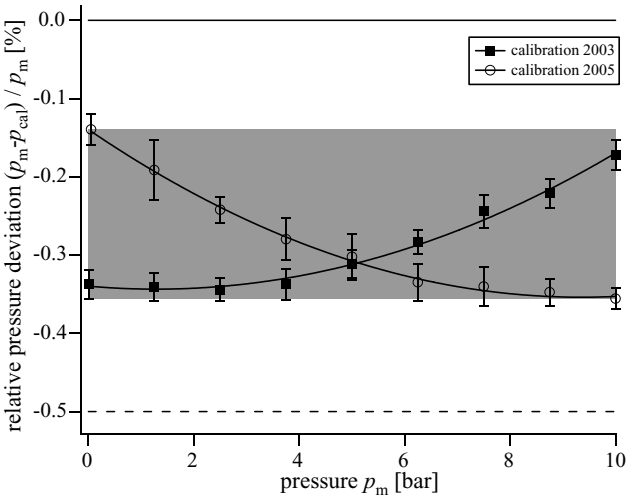

Fig. 8. Relative deviation and measurement uncertainty of the pressure transducer signal as found during the calibrations in 2003 and 2005. A parabola fit to the 2003 calibration data points gives $f_{2003}(p_{\mathrm{m}}) = -0.340(14) - 0.0059(68) \cdot p_{\mathrm{m}} + 0.00229(66) \cdot p_{\mathrm{m}}^2$ which was used to determine the actual cell pressure p_{cal} from the EL74 readout p_{m}, cf. eq. (39). The drift range of the relative deviations as shown by the hatched box is smaller than 0.2% and has been used afterwards as a conservative estimate for the pressure measurements' uncertainty ($\pm 0.2\%$). The dashed line shows the measurement uncertainty as claimed by the manufacturer ($\Delta p/p = 0.4\%$).

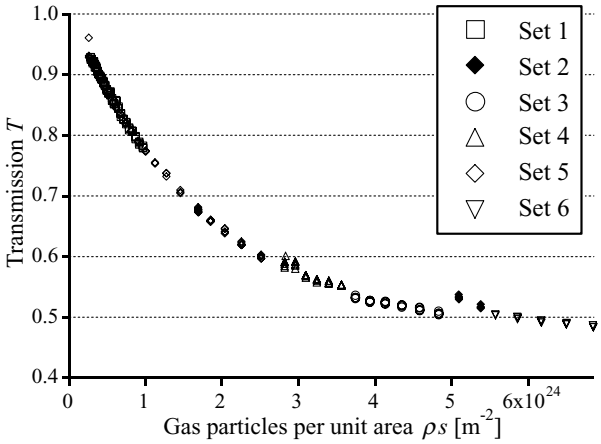

Fig. 9. Measured transmission $T = \frac{I_1 + \gamma \cdot I_2}{I_1 + I_2}$ as a function of gas particles per unit area. Errors lie within the data symbols.

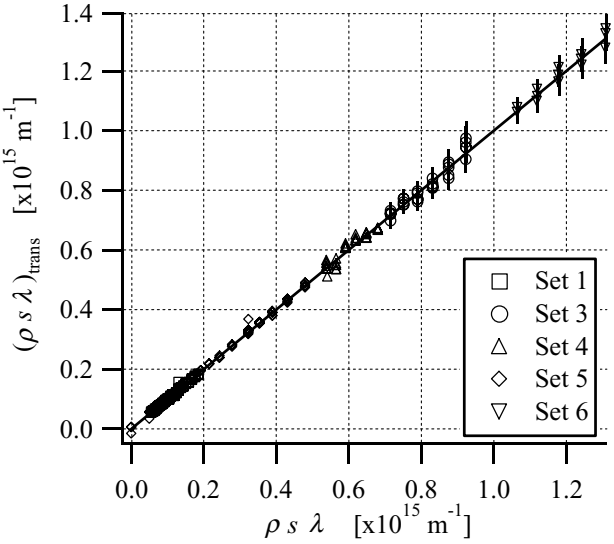

Fig. 10. The product $(\varrho s\lambda)_{\mathrm{trans},i}$ as calculated from transmission measurements *vs.* the same quantity from measurements of the individual quantities, *i.e.* the gas particle number density ϱ, the sample thickness s, and the neutron wavelength λ. Errors larger than the data symbols are printed as lines. The results of both measurement methods are in excellent agreement. The straight line shows the linear fit to the data.

fore, the data points are separated into six sets, which are defined by having been recorded without re-adjustments of the instrument. These data sets i are fitted exponentially to yield pairs of values for $\langle I_{1,2}\rangle$. Because Set 2 has been measured at essentially only two distinct pressure values, the exponential fit to this set is statistically insignificant and has been neglected in further analysis. Using eqs. (22) and (25) we can calculate the product $(\varrho s\lambda)_{\mathrm{trans},i} = \frac{1}{K_{\mathrm{a}}}\cdot\ln(T_i + \frac{\langle I_1\rangle_i}{\langle I_2\rangle_i}(T_i - 1))$. Note that the fitted values of $\langle I_{1,2}\rangle_i$ are insensitive to the scaling of the independent fit variable since they represent asymptotic values extracted from $T(\gamma = 0)$ and $T(\gamma \to \infty)$, cf. eq. (25). In fig. 10 the quantity $(\varrho s\lambda)_{\mathrm{trans},i}$ is plotted *vs.* the product term $(\varrho s\lambda)$.

One expects the data points to lie on the bisector if the measurements are consistent. A line fit $(\varrho s\lambda)_{\mathrm{trans}} = a_0 + b_0(\varrho s\lambda)$ to the data yields a constant a_0 which is zero within the error bars, a slope b_0 with excellent agreement to unity, and a reduced $\chi^2_\nu = 7$, which indicates that the uncertainty of the data might have been underestimated. This likely reflects the fact that the ratio I_1/I_2 is not constant during periods between re-adjustments of the apparatus. We conservatively account for this possible systematic error by re-estimating the uncertainties and multiplying them with a factor $\sqrt{7}$. We finally get

$$a_0 = -2(6) \times 10^{+11}\,\mathrm{m}^{-1},$$
$$b_0 = 1.000(3),$$
$$\chi^2_\nu = 1.$$

We conclude that the determination of $\varrho s\lambda$ through transmission measurements is not only consistent with the measurements of the individual quantities but yields a nearly identical uncertainty of ±3‰. For the analysis of the scattering length we use the values of the individual measurements for the determination of $(\varrho s\lambda)$ with its relative uncertainty of $\frac{\Delta(\varrho s\lambda)}{(\varrho s\lambda)} = \pm 3‰$, which is dominated by the relative uncertainties of both the pressure and wavelength measurements.

3.7 Measuring sequence

Before the first measurement was performed, the gas vessel was evacuated to a pressure p below 10^{-3} mbar and then filled with ^{3}He (^{3}He > 99.993%, ^{4}He < 0.007%, N_2 < 2 ppm, O_2 + Ar < 1 ppm, total hydrocarbons < 1 ppm, CO + CO_2 < 1 ppm, H_2 < 1 ppm, thereof $^3H_2 < 4.2 \times 10^{-8}$ ppm)[3]. Among the specified isotopes protons lead to the strongest shift of the samples' effective scattering length. A simple calculation shows that even a 7×10^{-3} admixture of protons would shift the measured scattering length by less than 7×10^{-4} fm and therefore was more than an order of magnitude smaller than the stated error of our result. The effect of the factual impurities is still much smaller. That is why the systematic error caused by gas impurities is negligible. After recording between three and five interferograms with and without sample, the gas particle number density was reduced slightly by opening a electropneumatic valve towards a vacuum pump for a short time. The stepwise reduction of the gas pressure ($\Delta p \approx 10, \ldots, 100$ mbar) was repeated until only a small quantity (< 100 mbar) of gas was left in the sample container. After another evacuation the cell was refilled with fresh ^{3}He gas. The whole procedure was repeated three times with initial ^{3}He pressures of $p = 1$ bar, 5.9 bar and 7.5 bar. In this way the phase shift due to the ^{3}He gas was measured as a function of the particle number density of the sample. A typical pair of interferograms is shown in fig. 2. The measured quantity is the phase shift of the sample interferogram with respect to the reference interferogram. Besides the attenuation of neutron intensity due to strong neutron absorption inside the ^{3}He volume, the phase shift is clearly visible.

4 Data analysis and results

For each pair of interferograms with and without sample, the phase shift was calculated by fitting harmonic functions to the data and computing the difference of the extracted phase constants. This technique is equivalent to the procedure described in sect. 3.1. Taking only Poisson statistics into account, the data are not described in a satisfactory way by cosine fits: a considerable number of data points, most notably in the edges of the cosine, deviate significantly from the fit function, see fig. 11. We typically get a reduced chi-squared of the order of ten. We assume that short-time phase fluctuations of the instrument are responsible for this behaviour. To take this error

[3] Purity according to the supplier CHEMGAS - 92100 Boulogne - France.

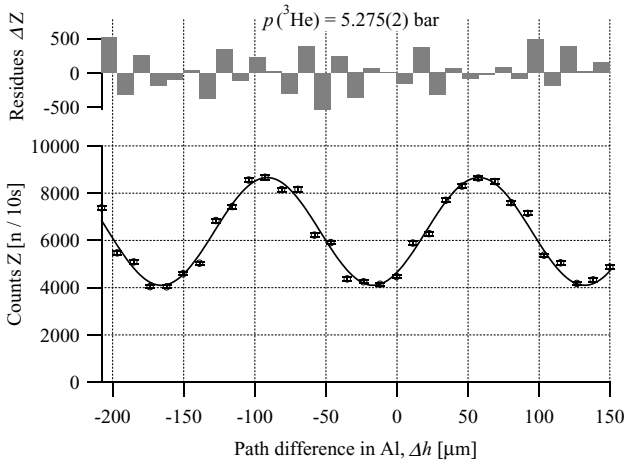

Fig. 11. If only Poisson statistics is taken into account, the interferogram's count rates are poorly described by cosine fits.

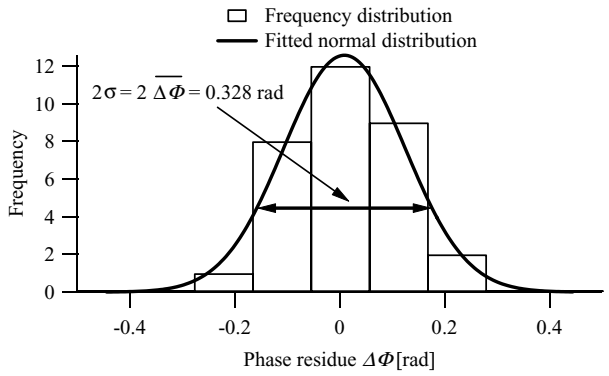

Fig. 12. The counting residuals are transformed into phase residuals and histogrammed. It turns out that the phase residuals are normally distributed to a good approximation.

contribution into account, we estimate the mean phase uncertainty of the individual data point in the following way: the expected count rates

$$Z = K_1 + K_2 \cos \Phi \tag{41}$$

are harmonic function of the phase Φ. The residuals of the individual data points with respect to the first fit are considered as phase residuals $\Delta\Phi$ instead of count rate residuals ΔZ. The analysis of the phase residuals $\Delta\Phi_i,\ i = \{1, \ldots, 32\}$ of every interferogram shows that these deviations are statistically distributed. Thus we may equate $\Delta\Phi_i$ with $g(t_i)$ from (29) since it satisfies[4] $\langle \Delta\Phi_i \rangle_T = 0$. We therefore assume that it is justified to take the standard deviation of the phase residuals as an estimate for the mean phase fluctuation $\overline{\Delta\Phi}$ of the individual data points, cf. fig. 12. In the next step, the mean count rate fluctuation $\overline{\Delta Z}$ *caused by the mean phase fluctuation* can be estimated:

$$\overline{\Delta Z} = K_2 \sin \Phi \times \overline{\Delta\Phi}. \tag{42}$$

[4] The reason for these statistical fluctuations of the intrinsic phase are tiny mechanical vibrations of < 1 Hz at the interferometer's suspension, which make their mark on the interferometer setup, resulting in short term fluctuations of the intrinsic phase.

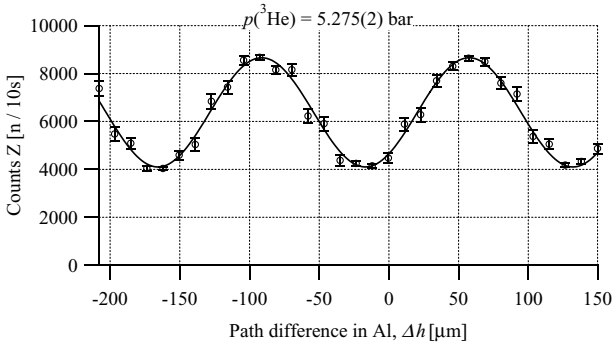

Fig. 13. The error at the single data points is re-estimated by adding quadratically the error due to Poisson counting statistics and the standard deviation of the intrinsic phase fluctuation.

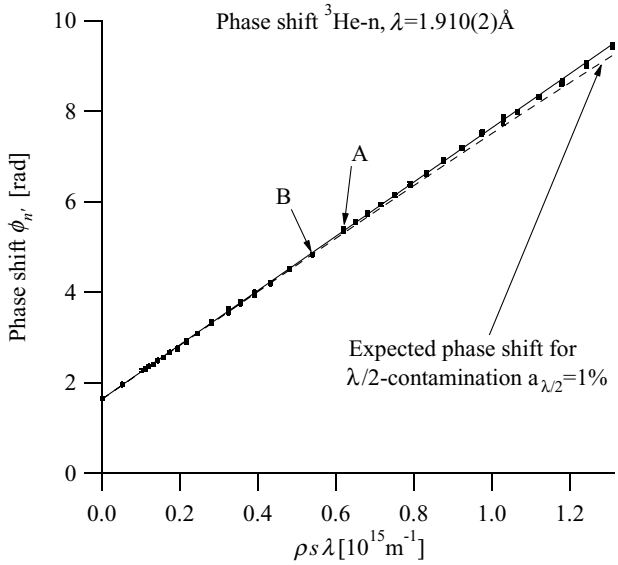

Fig. 14. Phase shift as a function of the particle number per unit area times the mean neutron wavelength $\varrho s\lambda$. Between the data points marked A and B, the experiment was interrupted for a 13 hour long maintenance break. The line is the result of a fit to the data using the model function (37). For a $\lambda/2$ contamination $a_{\frac{\lambda}{2}} = 1 - a_\lambda = 1\%$, the phase shift is expected to be described by the dashed curve.

By combining the Poisson statistics uncertainty and the phase fluctuation uncertainty of the count rates through Gaussian error propagation, we arrive at new estimates for the uncertainties of the individual count rates, see fig. 13. Fits to the data with improved count rate error estimates yield reduced chi-squared values which are very close to unity.

In fig. 14, the phase shifts of each pair of interferograms is plotted against the product of the particle number density ϱ times the effective sample thickness s, which was calculated from the thermodynamic state variables pressure p and temperature ϑ. The coherent scattering length

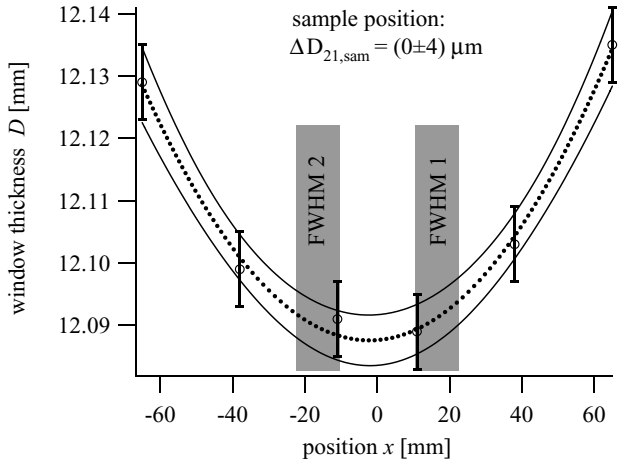

Fig. 15. Summed thickness of the entrance and exit aluminum windows as a function of the lateral position. The dotted line is a second-order polynomial fitted to the data, the full lines show an error interval of the fit which is in reasonable agreement with the errors of the individual data points. The FWHM (= 12 mm) of the partial neutron beams are shown as grey boxes. In the sample position, the partial neutron beams penetrate almost the same aluminum thickness.

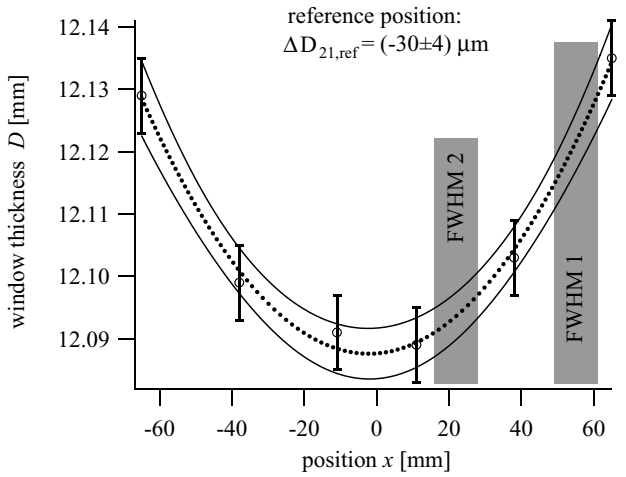

Fig. 16. In the reference position, partial neutron beam 1 travels a longer path through aluminum.

is obtained from a fit to the data, using the model function (37) and the relation (22). Herein, $\Phi_{n'}$ and $(\varrho s\lambda)$ are the dependent and independent variables, $b'_{\rm c}$ and a_λ are fit parameters, and $K_{\rm a}, k = 2\pi/\lambda, b''_{\rm c}$ are fixed constants[5]. The errors in $\Phi_{n'}$ and $(\varrho s\lambda)$ are assumed to be statistically independent. Therefore the errors in $(\varrho s\lambda)$ can be added to the error in $\Phi_{n'}$ by Gaussian error propagation:

$$\left(\Delta_{\rm fit}\Phi_{n'}\right)^2 = \left(\Delta\Phi_{n'}\right)^2 + \left(\Delta(\varrho s\lambda)\right)^2 .$$

We first note that the data show an almost linear dependence on ϱ, corresponding to only small higher-order wavelength contaminations. Secondly, the fit to the data obviously does not hit the origin. Instead, even if the sample chamber is empty, a phase shift of $\phi_{\rm int}^{\rm offset} = 1.626(4)$ rad is observed. This phase shift can be explained by a slightly biconcave shape of the aluminum windows which is a consequence of the mechanical production process. Figures 15 and 16 show a micrometer gauge measurement scan of the summed effective thicknesses of the entrance and exit windows. Also shown are the locations and the FWHMs of the two partial beams penetrating the aluminum windows with the cell in the sample and the reference position, respectively. To first approximation, the topology of the windows can be described by a second-order polynomial. Calculating the net optical path difference $\Delta D_{21,\rm n}$ of the two partial beams, linear error propagation has been used as a conservative error estimate. As can be inferred from figs. 15 and 16, we have $\Delta D_{21,\rm sam} = 0(4)\,\mu$m and $\Delta D_{21,\rm ref} = -30(4)\,\mu$m for the respective optical path differences in the sample and the reference positions giving $\Delta D_{21,\rm n} = \Delta D_{21,\rm sam} - \Delta D_{21,\rm ref} = 30(8)\,\mu$m, where we have added the individual errors linearly. This eventually translates into an offset phase shift

$$\phi_{\rm int}^{\rm offset} = 2\pi D_{21,\rm n}/D_\lambda = 1.26(34)\,\text{rad},$$

which is in fairly good agreement with the observed value. Since the bound coherent scattering length is extracted from the slope of the curve, the offset phase does not have any influence on our final result.

The fit to the data yields a value for the bound coherent scattering length of

$$b'_{\rm c} = 6.010(21)\,\text{fm} \tag{43}$$

and a relative weight of λ neutrons in the initial beam

$$a_\lambda = 0.9994(2) \tag{44}$$

with an excellent reduced chi-squared of 1. It is noteworthy that between the measurements marked with the letters A and B we had a 13-hour long measurement break

[5] Due to the smallness of the correction term in $kb''_{\rm c}$, which is of the order 10^{-4}, the shift of k for changing λ/n admixtures has been neglected.

Table 2. Error budget. For the extraction of $b'_{\rm c}$ from the phase shift data, $(\varrho s\lambda)$ with its relative error of ±3‰ has been used. For completeness the errors of the transmission analysis $(\varrho s\lambda)_{\rm trans}$ are displayed in the second half of the table.

Parameter	Value	Relative σ	Ref.
d_H [Å]	1.92005	1×10^{-5}	[31]
λ [Å]	1.910	1×10^{-3}	
s [mm]	$38.017 + 0.002 \cdot p$ [bar]	2×10^{-4}	
$\Delta p/p$	2×10^{-3}		
$\Delta\vartheta/\vartheta$	2×10^{-3}		
$\Delta\varrho/\varrho$	3×10^{-3}		
$\frac{\Delta(\varrho s\lambda)}{(\varrho s\lambda)}$	3×10^{-3}		
a_λ	0.9994	2×10^{-4}	
$(\varrho s\lambda)_{\rm trans}$	$a_0 + b_0(\varrho s\lambda)$		
a_0 [m^{-1}]	-2×10^{11}	3	
b_0	1.000	3×10^{-3}	
$\frac{\Delta(\varrho s\lambda)_{\rm trans}}{(\varrho s\lambda)_{\rm trans}}$	3×10^{-3}		

in which the twin cell was completely removed from the apparatus. The fact that the data join seamlessly at the points A and B underlines the effectiveness of our phase error compensation scheme.

Table 2 summarizes the parameters and relative uncertainties of all parameters used to extract b'_c from the measured phase shifts (fig. 14) by using eq. (37).

5 Discussion

Our result $b'_c = 6.010(21)$ fm represents almost an order-of-magnitude improvement in accuracy over the previous measurement of b'_c of Kaiser *et al.* [9]. The value differs by 4σ standard deviations with respect to [9]. Very recently, another group published a value for the same quantity with an improved measurement precision as well [34], which is $b'_c = 5.853(7)$ fm. Both experiments confirm that [9] underestimates b'_c. However, a clear discrepancy between our result and the value for the n-^{3}He bound coherent scattering length in [34] is the finding: They differ by more than 7 standard deviations within their quoted error bars. Therefore it seems reasonable to suppose that still a hidden systematic error might not have been considered yet. To trace out possible sources for this systematic discrepancy goes beyond the scope of this article and is a matter of future precision measurements in this field. Both experiments determined b'_c using neutron interferometric techniques. It should be pointed out, however, that two striking differences characterize the experimental setups used and the way b'_c was extracted from the recorded interferograms. Whereas the group at NIST used a symmetrically shaped perfect crystal silicon interferometer, the interferometer in our measurements at ILL was of the same kind, but skew-symmetrically shaped. Furthermore, by varying the sample pressure we introduced an additional degree of freedom to extract b'_c; at the same time the pressure variation gave us a direct experimental access to possible $\lambda/2$-contaminations of the neutron beam. At NIST the cell pressure was kept constant during the experiment.

Now, taking the value for b'_c, eq. (43), and further using eq. (2) and $b = \frac{m_n}{\mu}a$, our experimental result transforms into a linear combination of the singlet and triplet free scattering lengths a_- and a_+, which are plotted in fig. 17 together with the results from different earlier measurements of the coherent and incoherent scattering lengths of the n-^{3}He system. The recent value of the n-^{3}He bound incoherent scattering length, $b'_i = -2.365(20)$ fm ($a'_i = -1.772(15)$ fm), which was determined using pseudomagnetic precession in a polarized target placed in a neutron spin echo spectrometer [13], gives an almost orthogonal linear combination when plotted into the same multiplet scattering length plane. From the intersection point with the error band of our experimental value, new precise values for the singlet and triplet free scattering lengths can be derived:

$$a_- = 7.573(30)\,\text{fm} \qquad \text{and} \qquad a_+ = 3.480(18)\,\text{fm} \quad (45)$$

or

$$b_- = 10.106(40)\,\text{fm} \qquad \text{and} \qquad b_+ = 4.644(24)\,\text{fm} \quad (46)$$

for the corresponding bound multiplet scattering lengths. In order to compare our numbers with the published data in this field, the experimental error bands of the old data from Kaiser *et al.* [9], and the new precision value of b'_c from NIST [34], as well as the results from unpolarized bound scattering cross-section σ_s measurements with

$$\sigma_s = 4\pi\left(|b_c|^2 + |b_i|^2\right),$$

cf. eq. (12a) from Alfimenkov *et al.* [10] and Guckelsberger *et al.* are included in fig. 17.

Our result is close to very recently published predictions of Hofmann and Hale [14], which are based on microscopic calculations of n-^{3}He scattering with an underlying Argonne v_{18} nucleon-nucleon potential with and without integration of the three-nucleon potentials Urbana IX and V_3^*. Among these models, the potential Av_{18}+UIX reproduces best the experimental values for the binding energy, the threshold energy for neutron separation as well

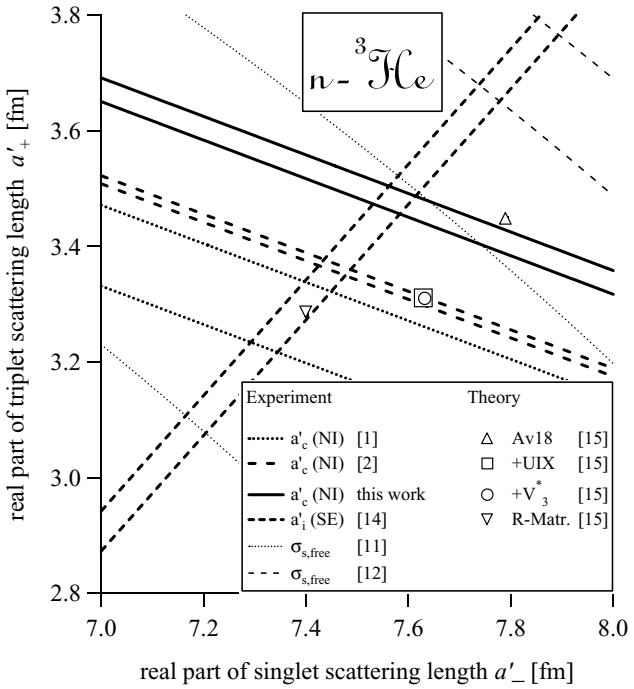

Fig. 17. Results of different measurements (NI: neutron interferometry, SE: spin echo spectroscopy) of the coherent and incoherent scattering lengths of the n-^{3}He system plotted in the multiplet scattering length plane. Measurements of the coherent scattering length result in linear combinations of the triplet and singlet scattering length with negative slope. Measurements of the incoherent scattering length hitherto yield almost orthogonal linear combinations. The result most recently measured by [34] differs by as much as 7σ (standard deviations) from the result reported here. However, both measurement exhibit a trend towards a higher value for b'_c as was reported by [9]. The predictions for the multiplet scattering lengths based on the modern Argonne v_{18} potential recently published by [14] are also shown.

as the imaginary parts $a''_{\pm}$ of the free multiplet scattering lengths. The discrepancy with regard to the Faddeev-Yacubovsky calculations in [35] and [3] may possibly vanish when three-body forces and the Coulomb interaction are taken into account in the calculations.

One of us (W.K.) has been funded by a grant of the DFG under contract number OT 33/17.

References

1. E.O. Alt, B.L.G. Bakker, Z. Phys. A **273**, 37 (1975).
2. K. Schoen, D.L. Jacobson, M. Arif, P.R. Huffman, T.C. Black, W.M. Snow, S.K. Lamoreaux, H. Kaiser, S.A. Werner, Phys. Rev. C **67**, 044005 (2003).
3. V.F. Kharchenko, V.P. Levashev, Nucl. Phys. A **343**, 249 (1980).
4. S. Hammerschmied, H. Rauch, H. Clerc, U. Kischko, Z. Phys. A **302**, 323 (1981).
5. H. Rauch, D. Tuppinger, H. Wölwitsch, T. Wroblewski, Phys. Lett. B **165**, 39 (1985).
6. M. Viviani, S. Rosati, A. Kievsky, Phys. Rev. Lett. **81**, 1580 (1998).
7. F. Ciesielski, J. Carbonell, C. Gignoux, Phys. Lett. B **447**, 199 (1999).
8. J. Als-Nielsen, O. Dietrich, Phys. Rev. **133**, 925 (1964).
9. H. Kaiser, H. Rauch, G. Badurek, W. Bauspiess, U. Bonse, Z. Phys. A **291**, 231 (1979).
10. V.P. Alfimenkov, G.G. Akopyan, J. Wierzbicki, A.M. Govorov, L.B. Pikel'ner, É.I. Sharapov, Sov. J. Nucl. Phys. **25**, 607 (1977) (originally published in Yad. Fiz. **25**, 1145 (1977)).
11. K. Guckelsberger, W. Nistler, R. Scherm, M. Weyrauch, Physica B **276-278**, 975 (2000).
12. K. Guckelsberger, Internal report of the PTB Laboratory 7.43 (2001).
13. O. Zimmer, G. Ehlers, B. Farago, H. Humblot, W. Ketter, R. Scherm, EPJdirect A **4**, 1 (2002), `http://www.edpsciences.org/articles/epjdirect/abs/2002/01/contents/contents.html`.
14. H.M. Hofmann, G.M. Hale, Phys. Rev. C **68**, 021002(R) (2003).
15. L. Koester, W. Nistler, Z. Phys. A **272**, 189 (1975).
16. L. Koester, in *Ergebnisse der exakten Naturwissenschaften*, edited by G. Höhler, Vol. **80**: *Neutron Physics* (Springer, Berlin, 1977) pp. 1-55.
17. V.E. Krohn, G.R. Ringo, Phys. Rev. **148**, 1303 (1966).
18. J.S. Meier, *Die Bestimmung der kohärenten gebundenen Streulänge gasförmiger Proben durch Kleinwinkelstreuungsmessungen an Hochdruck-Christiansenfiltern*, PhD Thesis, Technische Universität München (1985).
19. H. Rauch, in *Bergmann Schaefer – Lehrbuch der Experimentalphysik*, edited by H. Niedrig, Vol. **3**: *Optik*, 9th edition (Walter de Gruyter, Berlin, 1993).
20. H. Rauch, S.A. Werner, *Neutron Interferometry - Lessons in Experimental Quantum Mechanics*, 1st edition (Oxford University Press, Oxford, 2000).
21. M.L. Goldberger, F. Seitz, Phys. Rev. **71**, 294 (1947).
22. V.F. Sears, Phys. Rep. **82**, 1 (1982).
23. V.F. Sears, *Neutron Optics* (Oxford University Press, New York, Oxford, 1989).
24. G. Baym, *Lectures on Quantum Mechanics* (Addison Wesley, Reading, Mass., 1990) pp. 197-201.
25. E. Feenberg, Phys. Rev. **40**, 40 (1932).
26. V.F. Sears, Neutron News **3**, 26 (1992).
27. H. Rauch, W. Treimer, U. Bonse, Phys. Lett. A **47**, 369 (1974).
28. H. Rauch, Phys. Bl. **50**, 439 (1994).
29. H. Rauch, Phys. J. (Weinheim) **7**, 39 (2004).
30. G. Kroupa, G. Bruckner, O. Bolik, M. Zawisky, M. Hainbuchner, G. Badurek, R.J. Buchelt, A. Schricker, H. Rauch, Nucl. Instrum. Methods A **440**, 604 (2000).
31. L.I. Berger, B.R. Pamplin, in *CRC Handbook of Chemistry and Physics*, edited by D.R. Lide, 74th edition (CRC Press, Boca Raton, 1993-1994).
32. V.F. Sears, F.C. Khanna, Phys. Lett. B **56**, 1 (1975).
33. V.F. Sears, private communication with K. Guckelsberger 1991.
34. P.R. Huffman, D.L. Jacobson, K. Schoen, M. Arif, T.C. Black, W.M. Snow, S.A. Werner, Phys. Rev. C **70**, 014004 (2004).
35. V.F. Kharchenko, V.P. Levashev, Phys. Lett. B **60**, 317 (1976).